International Journal of Non-Linear Mechanics 46 (2011) 772–781

Contents lists available at ScienceDirect

International Journal of Non-Linear Mechanics

journal homepage: www.elsevier.com/locate/nlm

Bifurcations and chaos in large-Prandtl number Rayleigh–Bénard convection

Supriyo Paul [a], Pankaj Wahi [b,*], Mahendra K. Verma [a]

[a] Department of Physics, Indian Institute of Technology, Kanpur 208 016, India
[b] Department of Mechanical Engineering, Indian Institute of Technology, Kanpur 208 016, India

ARTICLE INFO

Article history:
Received 17 July 2010
Received in revised form
24 February 2011
Accepted 24 February 2011
Available online 4 March 2011

Keywords:
Rayleigh–Bénard convection
Bifurcation and chaos
Low-dimensional model

ABSTRACT

Rayleigh–Bénard convection with large-Prandtl number (P) is studied using a low-dimensional model constructed with the energetic modes of pseudospectral direct numerical simulations. A detailed bifurcation analysis of the non-linear response has been carried out for water at room temperature ($P=6.8$) as the working fluid. This analysis reveals a rich instability and chaos picture: steady rolls, time-periodicity, quasiperiodicity, phase locking, chaos, and crisis. Our low-dimensional model captures the reappearance of ordered states after chaos, as previously observed in experiments and simulations. We also observe multiple coexisting attractors consistent with previous experimental observations for a range of parameter values. The route to chaos in the model occurs through quasiperiodicity and phase locking, and attractor-merging crisis. Flow patterns spatially moving along the periodic direction have also been observed in our model.

1. Introduction

In this paper, we study various instabilities and chaos for large-Prandtl number (large-P) convection using bifurcation analysis. A low-dimensional model which captures several interesting features of previous experiments and simulations has been employed for the analysis.

Thermal convection in a fluid layer heated from below exhibits a host of complex phenomena including instabilities, patterns, chaos and turbulence [1–6]. An idealized and simple form of such system, the Rayleigh–Bénard convection (RBC), has been studied extensively due to its ability to show very rich dynamics. In RBC, a thin layer of fluid is confined between two thermally conducting horizontal plates that are separated by a distance d and heated from below (see Fig. 1). Non-dimensional parameters, Rayleigh number R and Prandtl number P dictate the fluid flow in RBC. P is defined as the ratio of kinematic viscosity ν and thermal diffusivity κ of the fluid, and $R=\alpha g\beta d^4/\nu\kappa$ is the ratio of buoyancy and dissipative forces, where α is the thermal expansion coefficient of the fluid, β is the temperature gradient imposed across the fluid layer, and g is the acceleration due to gravity. Increasing the temperature difference across the layer increases R and at a critical Rayleigh number R_c convection starts in the system as a result of a primary instability. R_c is independent of P, but it depends on the boundary conditions. In the case of no-slip boundary conditions where the fluid adjacent to the plates does not move (a realistic condition), the value of R_c is approximately 1708 [1]. For free-slip boundary conditions wherein there is no shear stress on the fluid from the plates and there is relative velocity between the fluid and the plates (an ideal condition), $R_c=657.5$ [1]. For a non-zero Prandtl number, the primary flow pattern at the onset of convection is always in the form of two-dimensional (2D) straight rolls [7]. The 2D rolls destabilize through secondary instabilities and they bifurcate into a sequence of dynamic patterns [6,8–11]. Generation of these secondary instabilities depend on the Prandtl number P.

The sequence of instabilities and onset of chaos are quite different for low-Prandtl number (low-P; $P\ll 1$) convection [12,13] and large-Prandtl number (large-P; $P\gtrsim 1$) convection [14–17]. For low-P convection, the 2D rolls become unstable close to the onset and wavy rolls are generated through secondary instabilities, thus making the flow three-dimensional (3D). These bifurcations and routes to chaos for low-P and zero-Prandtl number (zero-P) convection have been studied extensively (see [1–5,18–23] and references therein). The scenario however is quite different for large-P convection. The secondary instabilities are delayed here and the 2D rolls continue to be stable solutions till larger Rayleigh numbers. It has been reported that 2D convection results have significant similarities with 3D results for large-P convection [24,25]. We exploit this observation to analyze bifurcations and chaos for large-P convection using a low-dimensional model containing only 2D Fourier modes. A major advantage of this simplification is that the number of modes required for 2D convection is much fewer than 3D convection, thus enabling the bifurcation analysis.

Convection experiments (to be discussed in the next section) spanning over approximately four decades [8,14–16,26–31] reveal a

* Corresponding author.
E-mail addresses: supriyo@iitk.ac.in (S. Paul), wahi@iitk.ac.in (P. Wahi), mkv@iitk.ac.in (M.K. Verma).

0020-7462/$ - see front matter © 2011 Elsevier Ltd. All rights reserved.
doi:10.1016/j.ijnonlinmec.2011.02.010

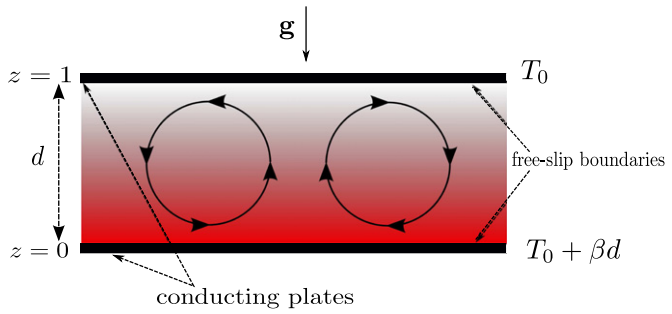

Fig. 1. Schematic representation of the two-dimensional RBC. T_0 is the temperature of the top plate. The bottom plate is at a higher temperature $T_0+\beta d$. β is the temperature gradient imposed between the plates and d is the distance between the plates. Due to heating, hot and lighter fluid near the bottom plate goes up while cold and heavier fluid comes down. This happens in the form of convection rolls represented by the circles here.

rich diversity of complex and interesting dynamics including several routes to chaos, travelling waves, and coexisting attractors. The findings of the experiments were reinforced by direct numerical simulations of both 2D and 3D convection [32–42]. Several attempts have also been made to understand the non-linear dynamics of RBC using appropriately constructed low-dimensional models [43–48]. These models mostly consist of the real Fourier modes and hence could not capture the travelling rolls and the associated dynamics. In contrast, we retain both real and imaginary components of the complex Fourier modes in our model, thus enabling us to capture spatially moving flow patterns associated with travelling waves. Our model also captures for the first time the reappearance of ordered states after chaos previously observed in DNS (see, e.g., [32,35,42]), and coexisting attractors reported in experiments [30].

For our analysis, we consider a box with an aspect ratio of $\Gamma_x=2\sqrt{2}$ and Prandtl number $P=6.8$ corresponding to water at room temperature, a representative of large-P fluid. A significant advantage of choosing this Prandtl number is that a large number of DNS [32,35,36,38,39] and experiments [14,16,26,27] have been performed for water. Our low-dimensional model contains 30 Fourier modes (14 complex modes and 2 real modes). We numerically advance the fixed points, limit cycles, and chaotic attractors to obtain a detailed bifurcation picture. For the fixed points and limit cycles, we use a fixed arc-length based continuation scheme [49,50]. However for the aperiodic attractors, we use the states at the end of a simulation for a given Rayleigh number as initial conditions for the next Rayleigh number. The convective patterns – steady, periodic, quasiperiodic, and chaotic rolls – observed in DNS and experiments are captured in our low-dimensional model. We observe a quasiperiodic phase-locking route to chaos as well as a chaotic attractor through attractor-merging crisis.

The rest of the paper is organized as follows. A brief review of the relevant literature is provided in Section 2, followed by a description of the governing equations and the low-dimensional model in Section 3. Details of the various convective regimes, bifurcation scenario and routes to chaos associated with the low-dimensional model is presented in Section 4. The last section contains discussions and conclusions.

2. Literature review

2.1. Experiments

Extensive RBC experiments were carried out by Krishnamurti [26,27] on fluids of different Prandtl numbers ($1 \lesssim P \lesssim 10^4$). She studied transition from 2D convection to 3D convection and subsequent generation of oscillatory, chaotic, and turbulent convection as a function of R and P. Busse and Whitehead [8] also reported 3D convective patterns, namely 'zigzag instability' and 'cross-roll instability' in an experiment on silicon oil ($P\sim100$). Gollub and Benson [16] experimentally studied routes to chaos in RBC of water at two different Prandtl numbers $P=2.5$ and 5 (different Prandtl numbers obtained by changing the mean temperature of water) for two aspect ratios, $\Gamma=3.5,2.4$, and observed rich dynamics. They observed a quasiperiodic route to chaos via phase locking, a quasiperiodic route to chaos via generation of third frequency, a period-doubling route to chaos, and intermittency. In another experiment, Giglio et al. [14] observed a period-doubling route to chaos in their convective experiment on water at room temperature ($P\sim6.8$). Bergé et al. [15] observed intermittency in their RBC experiment for a fluid with $P=130$, while Ciliberto and Rubio [28] reported localized oscillations and travelling waves in RBC experiments with silicon oil. Morris et al. [29] discovered spatio-temporal chaos in RBC of silicon oil. Metcalfe [30] reported coexistence of patterns and different attractors in his experiments with liquid Helium. Recently Sugiyama et al. [31] performed convection experiment on water ($P=5.7$) in quasi-2D geometry to study flow reversals. They observed novel interplay between convection rolls leading to flow reversal which were captured in their 2D direct numerical simulations. These results indicate complex non-linear dynamics including chaos through several routes in RBC. They also emphasize on the fact that the secondary instabilities and routes to chaos depend on the geometry (aspect ratio) of the experiment as well as the fluid used (Prandtl number).

2.2. Simulations

Direct numerical simulations (DNS) of 2D and 3D RBC have been used to study various convective states including turbulence. Curry et al. [32] performed detailed 3D spectral DNS for $P=10$ under free-slip boundary conditions with a grid size of 16^3; they reported quasiperiodic route to chaos via phase locking. However on increasing the grid size ($32^2\times16$ and 32^3) they observe quasiperiodic route to chaos via the generation of a third frequency (Ruelle–Takens route). Nishikawa and Yahata [33] performed 3D DNS using a finite difference scheme on no-slip boundary conditions for $P=6$, $\Gamma_x=3$, and $\Gamma_y=1.5$. Later Yahata [34] used the same method to simulate RBC for $P=5$, $\Gamma_x=3.5$, and $\Gamma_y=2$. Both Nishikawa and Yahata [33] and Yahata [34] observed quasiperiodic routes to chaos. Yahata [34] also observed a frequency-locked state leading to a chaotic state. Mukutmoni and Yang [35] reported a numerical study of RBC with water ($P=2.5$, similar to one of the experiments of Gollub and Benson [16]) in a rectangular enclosure with insulated sidewalls. They observed a period-2 state after a periodic solution, but the route to chaos was through quasiperiodicity. However, on imposing symmetry of the velocity and temperature field about the mid-planes they observed a period-doubling route to chaos. They also observed periodic solutions after chaos. Recently Evstigneev et al. [40] performed numerical simulations of 3D RBC using the finite volume method and observed that the laminar-turbulent transition follows the subharmonic bifurcation cascade of quasiperiodic orbit or the limit cycle. They argued that the bifurcation cascades follow the Feigenbaum–Sharkowski–Magnitskii (FSM) scenario [51].

In two dimensions, Moore and Weiss [36] simulated $P=6.8$ RBC using a finite difference method with free-slip boundary conditions; they studied heat transport as a function of R. McLaughlin and Orszag [37] considered RBC in air ($P=0.71$) with no-slip boundary conditions; they obtained periodic, quasiperiodic, and chaotic states. Curry et al. [32] performed detailed DNS for $P=6.8$ in 2D and observed bifurcations leading to periodic oscillations with a single frequency → two frequencies → single frequency. Goldhirsch et al. [38] also simulated 2D RBC and observed complex

behavior. Zienicke et al. [39] studied the effects of symmetries on 2D RBC using DNS and observed a quasiperiodic route to chaos via frequency locking. Recently, Paul et al. [41,42] performed 2D DNS for free-slip boundary conditions for a large range of Rayleigh numbers and obtained a quasiperiodic route to chaos. They also observed reappearance of steady and periodic convection beyond the chaotic state as well as travelling rolls. Thus, the qualitative behavior of the instabilities and chaos in large-P RBC captured by 2D and 3D DNS seems to match, thus making 2D RBC an important problem for the study of patterns and chaos in large-P convection. One noticeable difference between 2D RBC and 3D RBC is that the secondary instabilities in 2D RBC occur at significantly higher values of Rayleigh numbers than those in 3D RBC.

2.3. Low-dimensional models

Owing to the large number of modes present in DNS (even for moderate grid sizes) or experiments, the origin of various convective instabilities, patterns and chaos in DNS is not apparent. Interactions among large number of modes obscure the mechanism behind the bifurcations. This limitation however could be alleviated using low-dimensional models. A properly constructed low-dimensional model could capture the essential physics behind the bifurcations without the complications of large number of modes. Some of the earlier investigation of RBC using low-dimensional models are by Lorenz [43] and McLaughlin and Martin [44]. The Lorenz model containing only three modes is severely truncated and it captures only very basic dynamics of the RBC. McLaughlin and Martin [44] constructed a 39-mode model for $P=1$ and observed Ruelle–Takens like scenario for the advent of chaos. Curry [45] constructed a 14-mode model of RBC with small amplitude periodic modulations in the heat equation. He observed chaos for $P=10$. The low-dimensional model of Curry shows features similar to the experiments of Gollub and Benson [16], namely periodicity, quasiperiodicity, and chaos. Curry [46] also studied the 14-mode model without any modulations and found that the results are very similar to that of the Lorenz model wherein chaos appears as global chaos after a subcritical Hopf bifurcation. Yahata [47] studied transition to chaos in RBC using a 48-mode model under no-slip boundary conditions. For $P=5$, $\Gamma_x=2$ and $\Gamma_y=3.5$, he obtained periodic → quasiperiodic motion with two fundamental frequencies → quasiperiodicity with three frequencies → chaos. Yahata [48] continued the above analysis for $P=2.5$ with the same aspect ratio and reported period-doubling route to chaos.

Most of these models contained only the real components of the Fourier modes and hence could not capture the travelling wave type solutions observed both in experiments and DNS. In our model, we retain both the real and imaginary components of the complex Fourier modes enabling us to capture the travelling wave type of solutions. We also capture several features of previous DNS and experiments like reappearance of ordered states after chaos which were not captured by the earlier models. The bifurcation study using the low-dimensional models of Curry [45] and Yahata [47,48] vary the control parameter, the Rayleigh number, in discrete steps, thus they tend to miss some of the dynamics occurring in narrow windows. The bifurcation points cannot be precisely located in their model as well. In the present paper we numerically advance the fixed points, limit cycles, and chaotic attractors using a fixed arc-length based continuation scheme [49,50] for the fixed points and limit cycles, and using the states on an attractor for a given Rayleigh number as initial conditions for the next Rayleigh number for aperiodic attractors. As a result, a detailed bifurcation scenario emerges compared to those obtained by studying patterns at selected Rayleigh numbers. The approach in the present paper is very similar to a recent work by Pal et al. [23] and Mishra et al. [21] where they construct detailed bifurcation diagrams for zero-P and low-P convection respectively using the most energetic modes of DNS.

3. The low-dimensional model and associated flow patterns

3.1. Governing equations for RBC

In RBC, a thin layer of fluid is confined between two thermally conducting horizontal plates that are separated by a distance d (see Fig. 1). The bottom plate is maintained at a higher temperature than the top plate causing an adverse temperature or equivalently density gradient which gives rise to the instability. We assume Boussinesq approximation for the fluid [1]. The relevant hydrodynamic equations are non-dimensionalized using the length scale d, the large-scale velocity scale $\sqrt{\alpha\beta g d^2}$, and the temperature scale βd to yield [1]

$$\partial_t \mathbf{v} + (\mathbf{v}\cdot\nabla)\mathbf{v} = -\nabla p + \theta\hat{z} + \sqrt{\frac{P}{R}}\nabla^2\mathbf{v}, \tag{1}$$

$$\partial_t \theta + (\mathbf{v}\cdot\nabla)\theta = v_3 + \frac{1}{\sqrt{PR}}\nabla^2\theta, \tag{2}$$

$$\nabla\cdot\mathbf{v} = 0, \tag{3}$$

where $\mathbf{v}=(v_1,v_2,v_3)$ is the velocity fluctuation, θ is the perturbation in the temperature field from the steady conduction state, and $\hat{z}$ is the buoyancy direction. Non-dimensionalization using this kind of scaling [52] has some advantages over other commonly practiced scalings [53]. For example, the allowed time step is of the order of one, and the absolute values of large-scale velocity are not very large for large Rayleigh numbers. These enable more accurate numerical results for large R cases. As mentioned earlier, the non-dimensional parameters Rayleigh number R and Prandtl number P dictate the fluid flow in RBC. In this work, we fix the Prandtl number and study the variations in the flow pattern as the Rayleigh number is varied. In the present paper we use the reduced Rayleigh number $r=R/R_c$ as the control parameter.

The above equations are often solved using direct numerical simulations (DNS). One of the popular numerical techniques is the pseudospectral method in which the velocity and the temperature fields are expanded in the Fourier/Chebyshev basis functions. These numerical simulations have been able to reproduce various patterns, chaos, and turbulence observed in experiments. Convection simulations are however very expensive in terms of computer time and memory. In 3D DNS, the number of modes required to resolve the flow is $N\sim Re^{9/4}$ [54], where Re is the Reynolds number. The Reynolds number for large-P RBC is around $Re\sim R^{1/2}$ [55]. Therefore, the number of modes required for a convection simulation are approximately $N\sim R^{9/8}$. For a typical convective flow of interest, $R\sim 10^4$ for which $N\sim 10^4$, which is quite large. Simulation of such a flow with large number of modes is computationally very expensive. Also these large number of modes in DNS obscures the internal dynamics. A popular method to analyze such systems is a bifurcation analysis of an appropriately constructed low-dimensional system using the Fourier/Chebyshev modes. Using this technique we can study the origin of various patterns and chaos in RBC.

3.2. Low-dimensional model using Galerkin projection

For our low-dimensional model we choose 14 complex and two real Fourier modes to represent the large-scale flow structures. These modes are the most energetic modes of the DNS. They contribute almost 90% of the total energy of the system

collectively. These modes were chosen so as to capture most of the features of Paul et al.'s [42] simulation near the transition (for $r=1{:}50$). We also constructed models with fewer and larger number of modes. Models with fewer number of modes could not reproduce the salient features of DNS. We observed that our present model with 14 complex and two real modes was optimal. Models with larger number of modes showed almost identical features as our 30 mode model. Therefore, we stick to the present 30-mode model.

Expansion of the velocity fields v_1 and v_3, and the temperature field θ using the modes chosen for our model yields

$$\begin{aligned} v_1(x,z,t) = \frac{i\pi}{k_c}\Big[& W_{101}\exp(ik_cx)\cos(\pi z) + 3W_{103}\exp(ik_cx)\cos(3\pi z) \\ & + 5W_{105}\exp(ik_cx)\cos(5\pi z) + W_{202}\exp(2ik_cx)\cos(2\pi z) \\ & + \frac{1}{3}W_{301}\exp(3ik_cx)\cos(\pi z) + W_{303}\exp(3ik_cx)\cos(3\pi z) \\ & + \frac{1}{5}W_{501}\exp(5ik_cx)\cos(\pi z)\Big] + c.c., \end{aligned} \tag{4}$$

$$\begin{aligned} v_3(x,z,t) = {} & W_{101}(t)\exp(ik_cx)\sin(\pi z) + W_{103}(t)\exp(ik_cx)\sin(3\pi z) \\ & + W_{105}(t)\exp(ik_cx)\sin(5\pi z) + W_{202}(t)\exp(2ik_cx)\sin(2\pi z) \\ & + W_{301}(t)\exp(3ik_cx)\sin(\pi z) + W_{303}(t)\exp(3ik_cx)\sin(3\pi z) \\ & + W_{501}(t)\exp(5ik_cx)\sin(\pi z) + c.c., \end{aligned} \tag{5}$$

$$\begin{aligned} \theta(x,z,t) = {} & \theta_{101}(t)\exp(ik_cx)\sin(\pi z) + \theta_{103}(t)\exp(ik_cx)\sin(3\pi z) \\ & + \theta_{105}(t)\exp(ik_cx)\sin(5\pi z) + \theta_{202}(t)\exp(2ik_cx)\sin(2\pi z) \\ & + \theta_{301}(t)\exp(3ik_cx)\sin(\pi z) + \theta_{303}(t)\exp(3ik_cx)\sin(3\pi z) \\ & + \theta_{501}(t)\exp(5ik_cx)\sin(\pi z) + c.c. \\ & + \theta_{002}(t)\sin(2\pi z) + \theta_{004}(t)\sin(4\pi z), \end{aligned} \tag{6}$$

where *c.c.* stands for the complex conjugate, and the three subscripts denote the Fourier wavenumber indices along x, y, and z directions respectively. These modes correspond to the free-slip boundary condition for the velocity modes on the horizontal walls and periodic boundary conditions on the vertical walls. Note that the above modes represent two-dimensional rolls and hence there is no dependence of v_1, v_3 and θ on y, and

$$v_2(x,z,t) = 0. \tag{7}$$

The velocity field $\mathbf{v} \equiv (v_1, v_2, v_3)$ satisfies the incompressibility condition $\nabla \cdot \mathbf{v} = 0$ by construction. We choose $k_c = \pi/\sqrt{2}$ corresponding to the most unstable wavelength in RBC with free-slip boundary conditions. Hence the aspect ratio of our model is $2\sqrt{2}$. A Galerkin projection of Eqs. (1) and (2) on these modes yields a set of 30 coupled ordinary differential equations (ODEs) for the real and imaginary parts of the Fourier modes. These 30 non-linear ODEs comprise our low-dimensional model.

As already mentioned, the chosen modes for our Galerkin projection represent two-dimensional rolls. It has been reported earlier that 2D and 3D convection have significant similarity for large-P flows [25]. This similarity is due to the fact that the secondary instabilities are delayed for large-P convection, and the 2D rolls continue to be stable solutions till larger Rayleigh numbers. Therefore we expect our low-dimensional model to capture the dynamics of large-P convection to a large extent. Our model with 2D

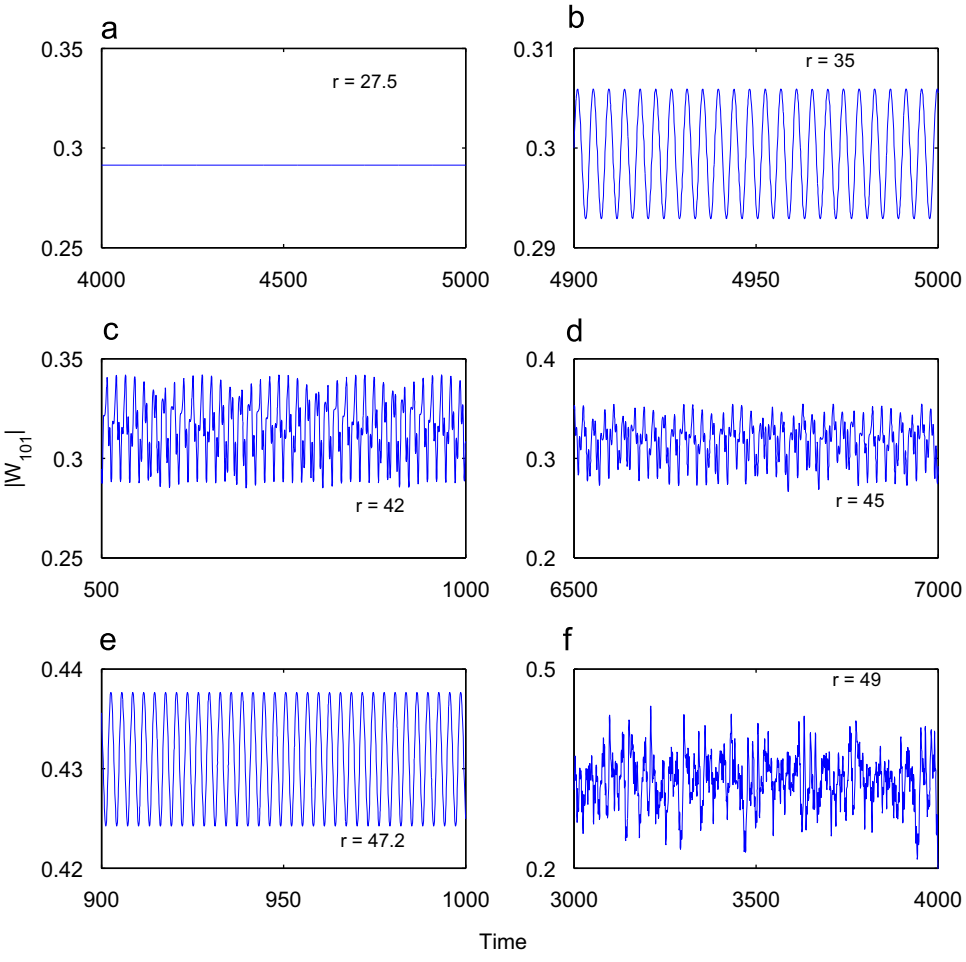

Fig. 2. Time series of the amplitude of the complex mode W_{101} generated by the low-dimensional model at various representative reduced Rayleigh numbers (r). We observe (a) steady convection ($r=27.5$), (b) time-periodic convection ($r=35$), (c) quasiperiodicity ($r=42$) and (d) chaos ($r=45$). Subsequently, (e) a window of time-periodic state ($r=47.2$) followed by (f) a chaotic state ($r=49$) is observed.

rolls has 30 modes, while a full 3D low-dimensional model would have many more modes that would make the bifurcation analysis of the model very difficult. Note that three-dimensional patterns like squares are not accessible to our model. However the origin of chaos and the sequence of bifurcations are expected to be common for both 2D and 3D convection for large-Prandtl number flows.

We note further that most of our modes are common to the low-dimensional model of Curry [45]. However, a major difference is that all the modes of our model are complex except θ_{002} and θ_{004} in contrast to Curry's model in which all the modes are real. Also, Curry had to include small amplitude modulations in his model to reproduce several of the patterns and chaos reported in the experiments of Gollub and Benson [16], whereas we do not require any such modulation or any additional forcing (other than buoyancy) to produce experimental patterns and chaos. In a related low-dimensional model, Yahata [47,48] studied RBC under no-slip boundary condition by expanding the velocity and temperature fields using mixed basis functions (Chebyshev along the buoyancy direction and Fourier along the horizontal directions) and observed similar behavior. Surprisingly the patterns and chaos reported for the no-slip and the free-slip boundary conditions are quite similar. However, Yahata's model does not show coexisting attractors and appearance of ordered states after chaos which is the one of the highlights of our low-dimensional model.

3.3. *Preliminary numerical simulations and associated flow patterns*

We numerically solve the low-dimensional model using random initial conditions. We use the fourth and fifth order Runge–Kutta solver of Matlab (ode45) to solve the system of ODEs. In our low-dimensional model, we observe various patterns: steady convection, periodicity, quasiperiodicity, and chaos at different values of Rayleigh numbers (see Fig. 2). Fig. 2 also shows that the system becomes periodic after chaos and then it becomes chaotic again. A curious feature of our model is that for the periodic solutions (r=27.6–40.3), the frequency of the Fourier amplitude is twice that of its phase (see Fig. 3). This feature along with the origin of the observed patterns can be understood using the bifurcation analysis which is the subject of the next section.

4. Bifurcation analysis of the low-dimensional model

In Fig. 4 we present a bifurcation diagram obtained by numerical integration of the low-dimensional model for P=6.8 and the aspect ratio of $2\sqrt{2}$. The reduced Rayleigh number r is the bifurcation parameter in our analysis. To generate this bifurcation diagram, numerical simulations of the model have been performed with a fixed initial condition till t=20 000 (large-scale eddy turnover time). Transients till t=5000 are eliminated and the extremum values of $|W_{101}|$ are plotted at later times. The stability and bifurcations of the steady states in this numerically generated bifurcation diagram are complemented by an eigenvalue analysis of the Jacobian evaluated at the fixed points, and the eigenvalue of the associated Floquet matrix for the limit cycles. For this complementary analysis, a fixed point is obtained numerically using the Newton–Raphson method for a given r, and the branches of the fixed points are subsequently obtained using a fixed

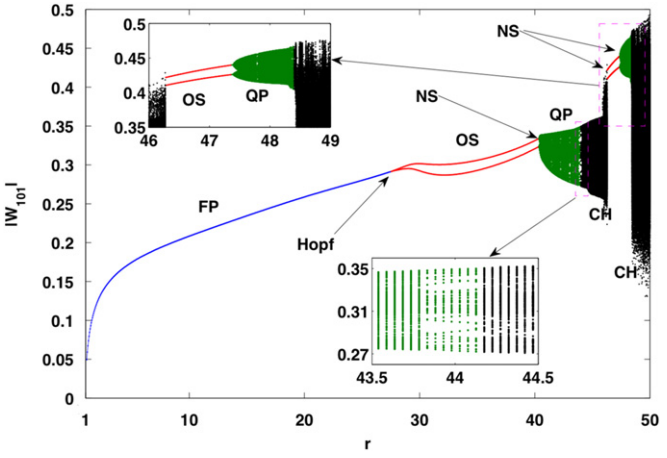

Fig. 4. Bifurcation diagram of the low-dimensional model representing large-Prandtl number RBC. 'FP' (blue curve) is the steady roll, 'OS' (red curve) is the time-periodic roll, 'QP' (green patch) is the quasiperiodic roll, and 'CH' (black patch) is the chaotic state. 'NS' indicates the Neimark–Sacker bifurcation point. A window of periodic and quasiperiodic states is observed in the band of r=46.2–48.4. (For interpretation of the references to color in this figure legend, the reader is referred to the web version of this article.)

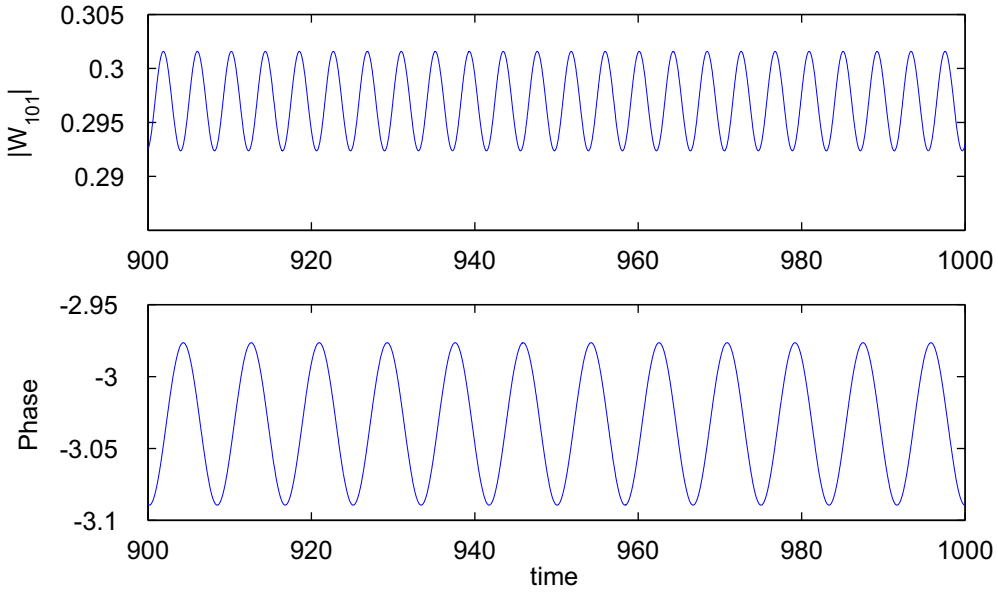

Fig. 3. Time-series of amplitude and phase of the complex W_{101} mode at r=30. The amplitude oscillates at double the frequency of its phase.

arc-length based continuation scheme (similar to the analysis in Pal et al. [23]).

For $r<1$, there is no convection in the system and heat is transported solely by conduction. The conduction state corresponds to the trivial fixed point of our system. At $r=1$, the system undergoes a pitch-fork bifurcation and time-independent convection states are born as non-trivial fixed points. Note that there are two non-zero solutions near the onset of convection (e.g., $\pm W_{101}$). These fixed point solutions are symmetric about the conduction solution. However these symmetries are observed only near the onset. In Fig. 4 we plot $|W_{101}|$ vs. r. The roll solutions (blue curve labeled 'FP') remain stable till $r\approx 27.6$.

The branch of fixed points corresponding to the steady convective rolls undergoes a supercritical Hopf bifurcation at $r=27.6$. As a consequence, the time-independent steady state becomes unstable and a time-periodic state (limit cycle) is born. The limits of $|W_{101}|$ for the limit cycle is indicated as the two red lines with the label 'OS' in the bifurcation diagram (Fig. 4). The two lines of 'OS' state designate the maxima and minima of $|W_{101}|$ respectively. The time variation of the modes is however more complex. As shown in Fig. 3, the amplitude of the mode W_{101} varies with a frequency twice that of its phase. This phenomena can be understood as follows. At the Hopf bifurcation point, the eigenvectors associated with the critical pair of purely imaginary eigenvalues $\pm i\omega$ have components only along the imaginary part of the Fourier modes (e.g., $\Im(W_{101})$). Hence, $\Im(W_{101})$ oscillates with the frequency ω corresponding to the Hopf point. The real parts of the Fourier modes are generated purely due to the quadratic non-linearities involving products of two imaginary parts of the modes; hence 2ω (superharmonic) is the leading frequency of the real parts and the amplitudes as well.

We determine the stability of the above time-periodic state using the Floquet theory. We numerically construct the fundamental (Floquet) matrix associated with the time-periodic state and compute its eigenvalues (called the 'Floquet multipliers'). All but one of the Floquet multipliers for a stable limit cycle have magnitude less than one (one Floquet multiplier is always one for an autonomous system). For an unstable limit cycle, at least one of them has a magnitude greater than one. When the Floquet multipliers cross the unit circle along the positive real axis, new limit cycles may appear or disappear ('pitchfork' or 'turning point' bifurcation). If they cross the unit circle along the negative real axis, the frequency of the limit cycle doubles in a 'period-doubling' bifurcation. However, a pair of complex-conjugate multipliers may also cross the unit circle in the complex plane, wherein another frequency is generated. This bifurcation is known as 'Neimark–Sacker' (NS) or a secondary Hopf bifurcation.

Fig. 5 illustrates the magnitude of the largest-in-magnitude Floquet multiplier as a function of the reduced Rayleigh number r, while Fig. 6 shows the movement of the Floquet multipliers in certain specific intervals of r. For evaluating the Floquet multipliers we proceed as follows. The limit cycle along with its time-period is obtained as a fixed point of an appropriately defined map (see [49,50]) using the Newton–Raphson method for a given r. The branch of limit cycles is subsequently computed using a fixed arc-length based continuation scheme. The fundamental matrix (and its eigenvalues) associated with the limit cycles for each value of r are then evaluated numerically by integrating the system of ODEs linearized about the limit cycle along with the full non-linear system.

Our computations reveal that the largest-in-magnitude Floquet multiplier has a magnitude of one up to $r\approx 40.3$ (till 'A' in Fig. 5), hence the limit cycle remains stable till $r\approx 40.3$. The system undergoes a Neimark–Sacker (NS) bifurcation near $r\approx 40.3$ as illustrated in Fig. 6(a). As a result of this NS bifurcation, a second frequency (incommensurate with the first one) is generated and the phase space trajectories show a transition from periodic orbits to

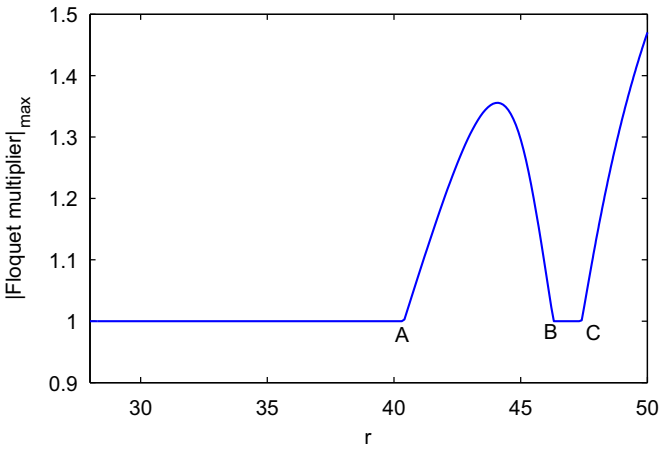

Fig. 5. The largest-in-magnitude Floquet multiplier of the low-dimensional system as a function of r. The largest-in-magnitude Floquet multiplier is greater than 1 beyond $r=40.3$ (point 'A') except in the 'BC' window in which we observe periodic states.

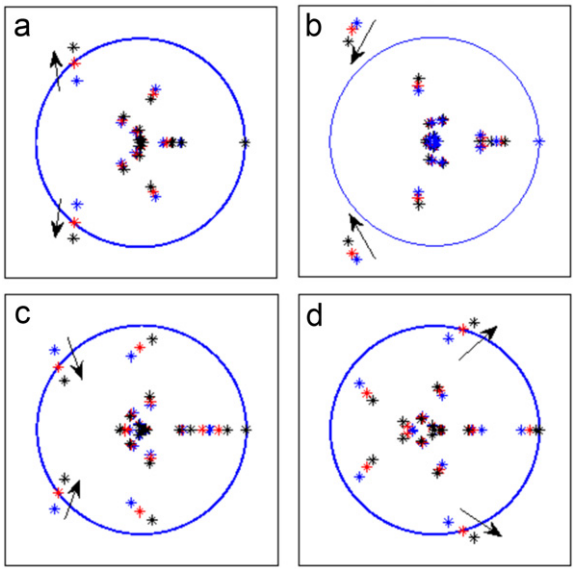

Fig. 6. Representation of the Floquet multiplier (FM) for various scenarios. Blue points indicate initial stage, red points indicate intermediate stage, and grey points indicate the final stage of the movement of the FM. (a) The FM crosses the unit circle through NS bifurcation ($r=40.3$) creating a quasiperiodic state. (b) The motion of the FM during the phase-locked regime ($r=43.8$–44.1). Note that the largest-in-magnitude FM remain outside the unit circle in this regime. (c) The largest-in-magnitude FM moves into the unit circle resulting in a periodic solution ($r=46.2$). (d) The largest-in-magnitude FM crosses the unit circle again creating a quasiperiodic solution ($r=47.4$). (For interpretation of the references to color in this figure legend, the reader is referred to the web version of this article.)

quasiperiodic orbits. The quasiperiodic state is shown as a green patch labeled 'QP' in the bifurcation diagram (Fig. 4). The phase space trajectories in this regime lie on a torus as illustrated in Fig. 7(a) for $r=42$. The power spectral density of the mode $|W_{101}|$ shown in Fig. 8(b) have two leading frequencies whose frequency ratio is approximately 3.099. To identify the leading frequency, the power spectral density for the periodic state is shown in Fig. 8(a).

As the bifurcation parameter r is increased further, the two frequencies get locked to yield a periodic solution whose phase trajectory lies on a torus as shown in Fig. 7(b) for $r=44$ (phase-locked state or resonant periodic movement on the torus). This occurs in a narrow window in Fig. 4 and its lower inset. The time-period of the periodic orbit shown in Fig. 7(b) is approximately

150 non-dimensional time units and the ratio of the two leading frequencies f_1/f_2 is approximately 3.152 ($\sim 167/53$). The corresponding movement of the Floquet multipliers is shown in Fig. 6(b) wherein the largest-in-magnitude Floquet multipliers are still outside the unit circle but they pass through a region which is at an angular location of approximately $2\pi/3$ from the real axis. The non-linearities in the system are strong enough for the two frequencies to get phase locked in this region. This scenario is very similar to that of the circle map [56]. The power spectrum of the mode W_{101} for the phase-locked state is illustrated in Fig. 8(c). Gollub and Benson [16] and Curry et. al. [32] report f_1/f_2 to be approximately 7/3 and 10/3 respectively for their phase-locked regime. Our $f_1/f_2 \approx 167/53$ is in general agreement with these earlier results.

With a further increase in the bifurcation parameter, the system becomes chaotic at around $r=44.2$. The route to chaos is similar to that in Curry–Yorke model [57, Section VIII.3] where chaos appears after quasiperiodicity in T^2 (2-Torus) and phase locking (see also [56, Section 6.7] for this scenario in a circle map). In the bifurcation diagram (Fig. 4), the chaotic region is shown by colored black patch labeled as 'CH'. As shown in Fig. 8(d) the power spectrum of the mode W_{101} is broadband indicating chaotic nature of the attractor. At around $r=45.9$, the size of the chaotic attractor suddenly increases as a result of an 'interior crisis'. This feature is illustrated in Fig. 9 where we plot the phase space projection on the $|W_{101}|-|W_{103}|$ plane at $r=45.8$ and 45.9.

The chaotic states after this interior crisis gives rise to flow patterns with chaotic movements of the primary roll structures, a travelling wave type solution (to be described in the next paragraph). The chaotic state described above exists till $r \lesssim 46.2$ after which we observe periodic solutions (the red curves in Fig. 4) that emerge from an inverse NS bifurcation. This inverse NS bifurcation is illustrated in Fig. 6(c) wherein the largest-in-magnitude Floquet multipliers enter into the unit circle making the limit cycles stable. This stable time-periodic orbit continues till $r=47.4$ at which point another pair of Floquet multipliers again crosses the unit circle in a forward NS bifurcation (see Fig. 6(d)) giving rise to a quasiperiodic state. In the periodic window the largest-in-magnitude Floquet multiplier is one

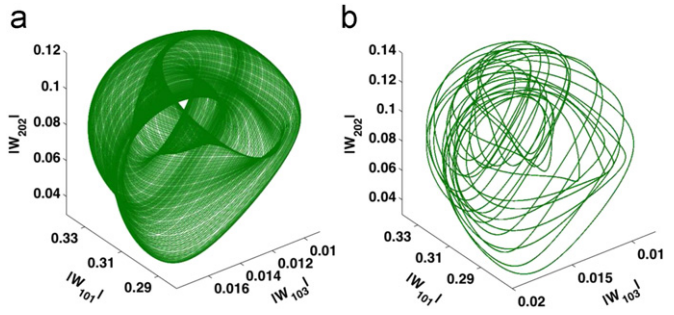

Fig. 7. A three-dimensional phase space projection of the phase space trajectories. (a) At $r=42$ the phase space trajectories fill the torus (quasiperiodic). (b) At $r=44$ the system is in a resonance periodic movement on torus (phase-locked state), and the phase space trajectory does not fill the torus (limit cycle).

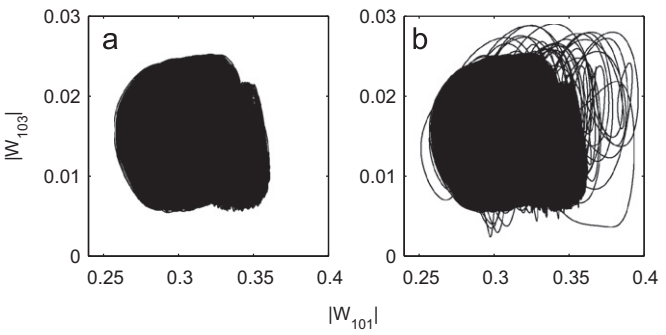

Fig. 9. The phase space projection on the $|W_{101}|-|W_{103}|$ plane of the chaotic attractor at (a) $r=45.8$ and (b) 45.9. The chaotic attractor shows a sudden increase in size at $r=45.9$.

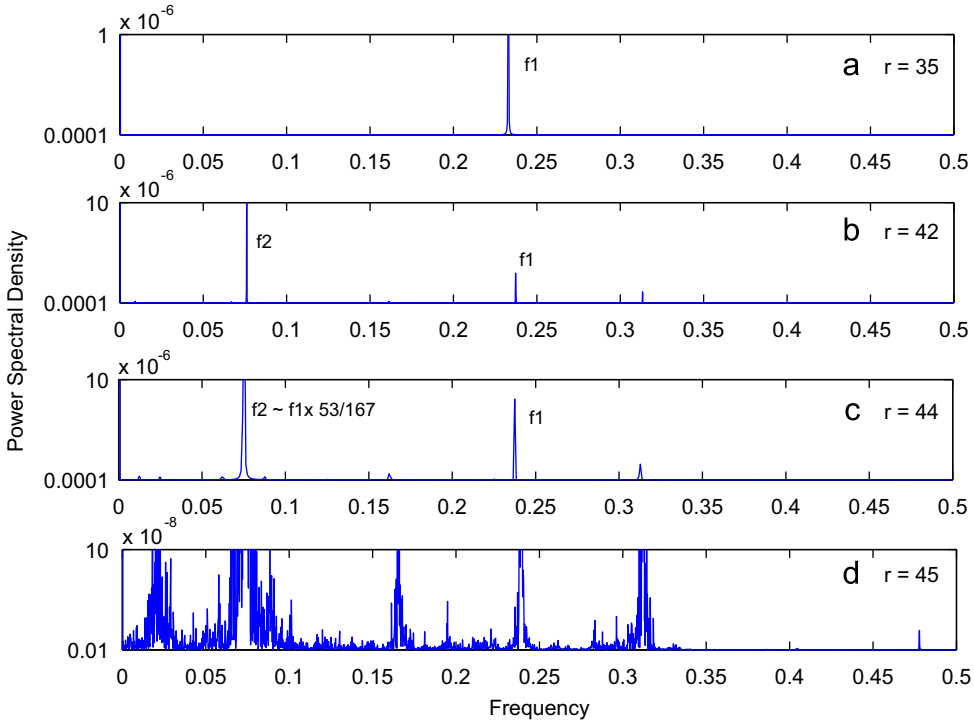

Fig. 8. The power spectral density of the mode W_{101} for various dynamical states: (a) periodic, (b) quasiperiodic ($f_1/f_2 \approx 3.099$), (c) phase locked ($f_1/f_2 \approx 3.152 \sim 167/53$), (d) chaos.

as illustrated by the 'BC' window in Fig. 5. This quasiperiodic state subsequently becomes chaotic at $r=48.4$ and the chaotic attractor continues for higher values of r. This chaotic attractor involves chaotic movement of the primary rolls as well. A zoomed portion of this regime of r is shown in the upper inset of Fig. 4. We also note that the size of the chaotic attractor after $r=48.4$ is much larger than the QP attractor. This feature can be explained using 'attractor-merging crisis' to be discussed later in this section.

We observe chaotic travelling rolls for $r=45.9$–46.2 and 48.4–50. The spatial motion of the primary roll structures can be attributed to the changes in the phase of the modes. Fig. 10 shows the phase space projection of the chaotic attractor on the $\Re(W_{101})-\Im(W_{101})$ plane for $r=46$ and 50. The phase of the W_{101} mode can take all the values in $(0,2\pi)$ and it changes chaotically. A change in phase of the mode translates into chaotic spatial motion of the corresponding flow pattern [41] in the periodic direction. This kind of motion has been observed earlier in DNS [41,42].

We discussed earlier that in the band $r=46.2$–48.4 the low-dimensional model has a periodic and a quasiperiodic attractor. However, in the same band of r a different set of initial conditions yield another attractor which is chaotic (see Fig. 11 depicting extrema of the mode $|W_{101}|$). The two coexisting attractors for $r=48.3$ (in the band $r=46.2$–48.4) have been shown in Fig. 12(a) with the green region as the QP attractor and the black region as the chaotic attractor. At $r=48.4$ these two attractors merge through an 'attractor-merging crisis' and form a single large attractor as shown

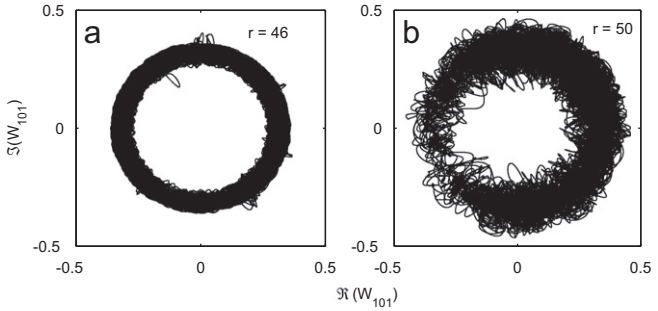

Fig. 10. Phase space projection of the chaotic attractor on the $\Re(W_{101})$ and $\Im(W_{101})$ plane at $r=46$ and 50. The phase of the mode W_{101} takes all the values in $(0,2\pi)$.

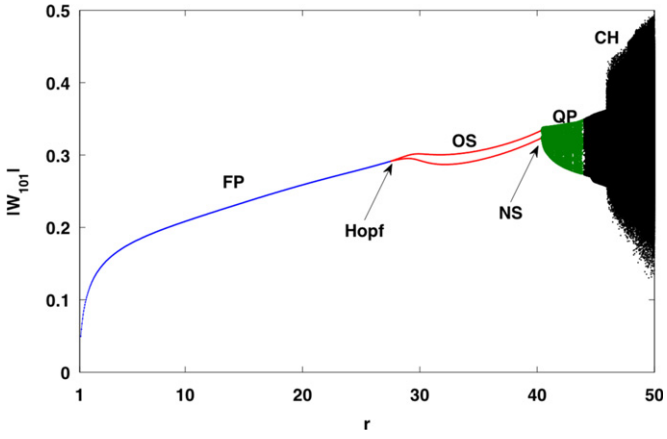

Fig. 11. Bifurcation diagram for the low-dimensional model with initial condition different from the one used for generating Fig. 4. 'FP' stands for fixed point state (blue), 'OS' stands for oscillatory state (red), 'QP' stands for quasiperiodic state (green) and 'CH' stands for chaotic state (black). 'NS' stands for the Neimark–Sacker bifurcation point. The present attractor and that of Fig. 4 differ for $r=46.2$–48.4. (For interpretation of the references to color in this figure legend, the reader is referred to the web version of this article.)

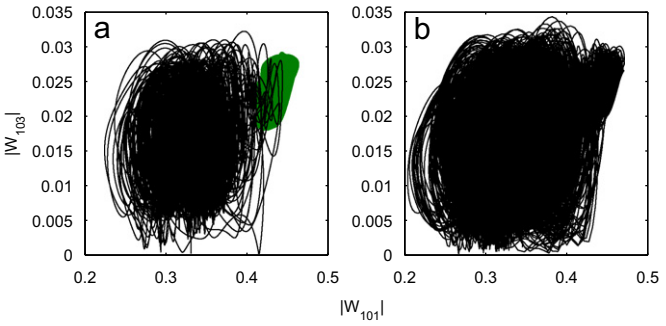

Fig. 12. The phase space projection on the $|W_{101}|-|W_{103}|$ plane at (a) $r=48.3$ and (b) 48.5. (a) At $r=48.3$, two attractors, a chaotic attractor (black patch) and a quasiperiodic attractor (green patch) coexist. These two attractors are accessible through two different initial conditions. (b) At $r=48.5$ the two attractor merges to generate a larger chaotic attractor. (For interpretation of the references to color in this figure legend, the reader is referred to the web version of this article.)

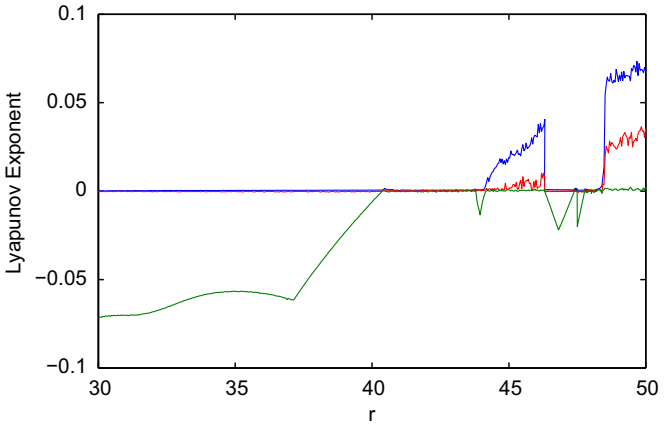

Fig. 13. Three largest Lyapunov exponents of the low-dimensional model corresponding to the attractors in Fig. 4.

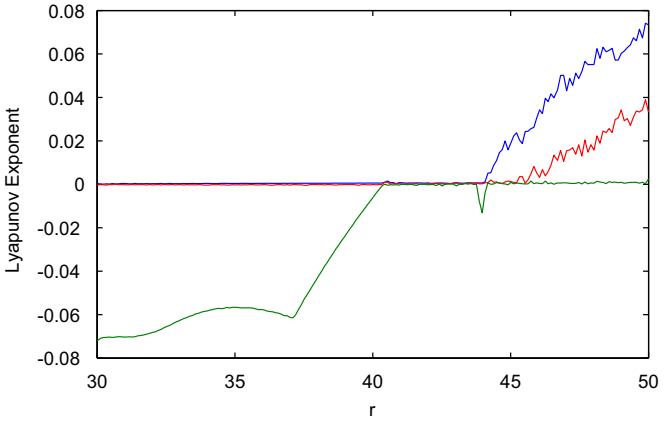

Fig. 14. Three largest Lyapunov exponents of the low-dimensional model corresponding to the attractors in Fig. 11.

in Fig. 12(b). The size of the resulting attractor is much larger than the original QP attractor but similar to that of the chaotic attractor of Fig. 11.

To ascertain the chaotic nature of the solutions obtained in our low-dimensional system, we compute the Lyapunov exponents associated with the various solutions presented in Figs. 4 and 11. The three largest Lyapunov exponents of our system corresponding to the attractors in Figs. 4 and 11 are shown in Figs. 13 and 14 respectively. There is at least one zero Lyapunov exponent

throughout the range consistent with the fact that our system is autonomous. In the chaotic regions described earlier there are two positive Lyapunov exponents clearly distinct from the zero exponent ascertaining the chaotic nature of the solutions. The largest Lyapunov exponents in Fig. 13 is zero for $r=46.2$–48.4 that corresponds to the periodic and quasiperiodic window shown in Fig. 4.

5. Discussions and conclusions

In this paper we present a bifurcation analysis of a 30-mode model for the Prandtl number $P=6.8$ (water at room temperature, a typical large-Prandtl number fluid) and aspect ratio $2\sqrt{2}$. In our bifurcation analysis we observe various patterns: steady rolls ($r=1$–27.6), time-periodic rolls ($r=27.6$–40.3), quasiperiodicity ($r=40.3$–43.8), phase-locked state ($r=43.8$–44.2), and chaos ($r>44.2$). Chaos occurs after quasiperiodicity and phase locking. Periodic and quasiperiodic rolls reappear after the chaotic state in the range of $r=46.2$–47.4 and $r=47.4$–48.4 respectively. After the second quasiperiodic window the system becomes chaotic again through an 'attractor-merging crisis'. A distinct feature of our analysis is that we track the fixed points, limit cycles, and chaotic attractors, thus getting a detailed bifurcation picture for the range of r under investigation.

Our low-dimensional model exhibits coexistence of several attractors. In the window of $r=46.2$–48.4, the system has periodic and quasiperiodic attractors along with a chaotic attractor. Coexistence of patterns and different attractors have been observed earlier in experiments [30]. Another novel feature of our low-dimensional model is that it reproduces reappearance of periodic rolls after chaos, a feature observed in the DNS of Curry et al. [32], Mukutmoni and Yang [35] and Paul et al. [42], albeit at different r values.

The route to chaos in our 30-mode model closely resembles some of the past experimental results on large-Prandtl number convection namely that of Gollub and Benson [16] who observed chaos in water for various Prandtl numbers and aspect ratios. The route to chaos in Gollub and Benson's experiment for $P=5$ and aspect ratio of 3.5 is through quasiperiodicity and phase locking. In direct numerical simulation of 3D RBC, Curry et al. [32] and Yahata [34] observed similar transition to chaos for $P=10$ and 5 respectively. Our low-dimensional model follows the same route to chaos. The range of Rayleigh numbers for our low-dimensional model is also quite close to the experiments of Gollub and Benson, and DNS of Curry et al. and Yahata. Thus our low-dimensional model captures the dynamics of 3D RBC responsible for transition to chaos through quasiperiodicity and phase locking.

Gollub and Benson [16] also reported chaos in their large-Prandtl number RBC through period-doubling, generation of three frequency (quasiperiodicity), and intermittency for different sets of Prandtl numbers and aspect ratios. Our preliminary investigation for $P=10$ and aspect ratio of $2\sqrt{2}$ appears to indicate intermittency, however, we need to study this phenomena more carefully. Some of the features reported by Gollub and Benson could possibly be captured by our model by varying the aspect ratio and the Prandtl number, a topic to be investigated in future. Further work is required in construction and analysis of more refined models for RBC to completely understand the mystery of the origin of the various flow patterns in convection.

Acknowledgment

We thank Krishna Kumar, Pankaj Mishra, and Pinaki Pal for useful discussion and K. Nandakumar for a careful reading of the manuscript. We also thank the anonymous reviewers for useful technical comments. Part of this work is supported by the grant of Swarnajayanti fellowship to MKV by Department of Science and Technology, India. Our model is motivated by DNS runs performed in EKA of Computational Research Laboratory (CRL), Pune. We thank CRL for providing us access to EKA.

References

[1] S. Chandrasekhar, Hydrodynamic and Hydromagnetic Stability, Cambridge University Press, Cambridge, 1961.
[2] F.H. Busse, Hydrodynamic instabilities and the transition to turbulence, in: H.L. Swinney, J.P. Gollub (Eds.), Topics in Applied Physics, vol. 45, Springer, Berlin, 1985, pp. 97–137.
[3] J.K. Bhattacharjee, Convection and Chaos in Fluids, World Scientific, Singapore, 1987.
[4] E. Bodenschatz, W. Pesch, G. Ahlers, Recent developments in Rayleigh–Bénard convection, Annu. Rev. Fluid Mech. 32 (2000) 709.
[5] P. Manneville, Instabilities, Chaos and Turbulence, Imperial College Press, London, 2004.
[6] M.C. Cross, P.C. Hohenberg, Rev. Mod. Phys. 65 (1993) 851.
[7] A. Schlütter, D. Lortz, F.H. Busse, On the stability of steady finite amplitude convection, J. Fluid Mech. 23 (1965) 129.
[8] F.H. Busse, J.A. Whitehead, Instabilities of convection rolls in a high Prandtl number fluid, J. Fluid Mech. 47 (1971) 305.
[9] F.H. Busse, Non-linear properties of thermal convection, Rep. Prog. Phys. 41 (1978) 1929.
[10] F.H. Busse, R.M. Clever, Instabilities of convection rolls in a fluid of moderate Prandtl number, J. Fluid Mech. 91 (1979) 319.
[11] G. Ahlers, 25 Years of nonequilibrium statistical mechanics, in: J.J. Brey, J. Marro, J.M. Rubí, M.S. Miguel (Eds.), Lecture Notes in Physics, Springer, Berlin, 1995, pp. 91–124.
[12] A. Libchaber, C. Laroche, S. Fauve, Period doubling cascade in mercury a quantitative measurement, J. Phys. Lett. 43 (1982) L211.
[13] A. Libchaber, S. Fauve, C. Laroche, Two-parameter study of the routes to chaos, Physica D 7D (1983) 73.
[14] M. Giglio, S. Musazzi, U. Perini, Transition to chaotic behavior via a reproducible sequence of period-doubling bifurcations, Phys. Rev. Lett. 47 (1981) 243.
[15] P. Bergé, M. Dubois, P. Manneville, Y. Pomeau, Intermittency in Rayleigh–Bénard convection, J. Phys. Lett. 41 (1980) L341.
[16] J.P. Gollub, S.V. Benson, Many routes to turbulent convection, J. Fluid Mech. 100 (1980) 449.
[17] J. Stavans, F. Heslot, A. Libchaber, Fixed winding number and the quasiperiodic route to chaos in a convective fluid, Phys. Rev. Lett. 55 (1985) 596.
[18] F.H. Busse, The oscillatory instability of convection rolls in a low Prandtl number fluid, J. Fluid Mech. 52 (1972) 97.
[19] M.R.E. Proctor, Inertial convection at low Prandtl number, J. Fluid Mech. 82 (1977) 97.
[20] R.M. Clever, F.H. Busse, Low-Prandtl-number convection in a layer heated from below, J. Fluid Mech. 102 (1981) 61.
[21] P.K. Mishra, P. Wahi, M.K. Verma, Patterns and bifurcations in low-Prandtl number Rayleigh–Bénard convection, Europhys. Lett. 89 (2010) 44003.
[22] K. Kumar, S. Fauve, O. Thual, Critical self-tuning: the example of zero Prandtl number convection, J. Phys. II (France) 6 (1996) 945.
[23] P. Pal, P. Wahi, M.K. Verma, S. Paul, K. Kumar, P.K. Mishra, Bifurcation and chaos in zero Prandtl number convection, Europhys. Lett. 87 (2009) 54003.
[24] A.P. Vincent, D.A. Yuen, Transition to turbulent thermal convection beyond $Ra=10^{10}$ detected in numerical simulations, Phys. Rev. E 61 (2000) 5241.
[25] J. Schmalzl, M. Breuer, U. Hansen, On the validity of two-dimensional numerical approaches to time-dependent thermal convection, Europhys. Lett. 67 (2004) 390.
[26] R. Krishnamurti, On the transition to turbulent convection. Part 1. The transition from two- to three-dimensional flow, J. Fluid Mech. 42 (1970) 295.
[27] R. Krishnamurti, On the transition to turbulent convection. Part 2. The transition to time-dependent flow, J. Fluid Mech. 42 (1970) 309.
[28] S. Ciliberto, M.A. Rubio, Chaos and order in the temperature field of Rayleigh–Bénard convection, Phys. Scr. 36 (1987) 920.
[29] S.W. Morris, E. Bodenschatz, D.S. Cannell, G. Ahlers, Spiral defect chaos in large aspect ratio Rayleigh–Bénard convection, Phys. Rev. Lett. 71 (1993) 2026.
[30] G. Metcalfe, R.P. Behringer, Convection in ^{3}He-superfluid-^{4}He mixtures. Part 2. A survey of instabilities, J. Fluid Mech. 307 (1996) 297.
[31] K. Sugiyama, et al., Flow reversals in thermally driven turbulence, Phys. Rev. Lett. 105 (2010) 034503.
[32] J.H. Curry, J.R. Herring, J. Loncaric, S.A. Orszag, Order and disorder in two- and three-dimensional Bénard convection, J. Fluid Mech. 147 (1984) 1.
[33] S. Nishikawa, H. Yahata, Evolution of the Rayleigh–Bénard convection in a rectangular box, J. Phys. Soc. Jpn. 65 (1996) 935.
[34] H. Yahata, Transition to chaos in the Rayleigh–Bénard convection, J. Phys. Soc. Jpn. 69 (2000) 1384.
[35] D. Mukutmoni, K.T. Yang, Rayleigh–Bénard convection in a small aspect ratio enclosure. II: bifurcation to chaos, J. Heat Transfer 115 (1993) 367.

[36] D.R. Moore, N.O. Weiss, Two-dimensional Rayleigh–Bénard convection, J. Fluid Mech. 58 (1973) 289.
[37] J.B. McLaughlin, S.A. Orszag, Transition from periodic to chaotic thermal convection, J. Fluid Mech. 122 (1982) 123.
[38] I. Goldhirsch, R.B. Pelz, S.A. Orszag, Numerical simulation of thermal convection in a two-dimensional finite box, J. Fluid Mech. 199 (1989) 1.
[39] E. Zienicke, N. Seehafer, F. Feude, Bifurcations in two-dimensional Rayleigh–Bénard convection, Phys. Rev. E 57 (1998) 428.
[40] N.M. Evstigneev, N.A. Magnitskii, S.V. Sidorov, Nonlinear dynamics of laminar-turbulent transition in three dimensional Rayleigh–Bénard convection, Commun. Nonlinear Sci. Numer. Simulat. 15 (2010) 2851.
[41] S. Paul, K. Kumar, M.K. Verma, D. Carati, A. De, V. Eswaran, Chaotic traveling rolls in Rayleigh–Bénard convection, Pramana 74 (2010) 75.
[42] S. Paul, M.K. Verma, P. Wahi, S.K. Reddy, K. Kumar, Chaotic dynamics in two-dimensional Rayleigh-Bénard convection, arXiv:1005.5517v1, 2010.
[43] E.N. Lorenz, Deterministic nonperiodic flow, J. Atmos. Sci. 20 (2) (1963) 130.
[44] J.B. McLaughlin, P.C. Martin, Transition to turbulence in a statistically stressed fluid system, Phys. Rev. A 12 (1975) 186.
[45] J.H. Curry, Chaotic response to periodic modulation of model of a convecting fluid, Phys. Rev. Lett. 43 (1979) 1013.
[46] J.H. Curry, A generalized Lorenz system, Commun. Math. Phys. 60 (1978) 193.
[47] H. Yahata, Transition to turbulence in the Rayleigh–Bénard convection, Prog. Theor. Phys. 68 (1982) 1070.
[48] H. Yahata, Period-doubling cascade in the Rayleigh–Bénard convection, Prog. Theor. Phys. 69 (1983) 1802.
[49] K. Nandakumar, A. Chatterjee, Resonance, parameter estimation, and modal interactions in a strongly nonlinear benchtop oscillator, Nonlinear Dyn. 40 (2005) 143.
[50] P. Wahi, A. Chatterrjee, Self-interrupted regenerative metal cutting in turning, Int. J. Nonlinear Mech. 43 (2008) 111.
[51] N.A. Magnitskii, S.V. Sidorov, New Methods for Chaotic Dynamics, World Scientific, Singapore, 2006.
[52] K. Koal, et al., Numerical experiments of turbulent thermal convection at high Rayleigh numbers, in: M. Oberlack, G. Khujadze, S. Günther, T. Weller, M. Frewer, J. Peinke, S. Joachim (Eds.), Progress in Turbulence II, Springer, Berlin, 2007, pp. 177–180.
[53] A.V. Getling, Rayleigh–Bénard Convection: Structures and Dynamics, World Scientific, Singapore, 1998.
[54] S.B. Pope, Turbulent Flows, Cambridge University Press, Cambridge, 2000.
[55] S. Grossman, D. Lohse, Thermal convection for large Prandtl numbers, Phys. Rev. Lett. 86 (2001) 3316.
[56] R.C. Hilborn, Chaos and Nonlinear Dynamics: An Introduction for Scientists and Engineers, Oxford University Press, Oxford, 1994.
[57] P. Bergé, Y. Pomeau, C. Vidal, Order Within Chaos, John Wiley & Sons, Paris, 1984.